

# Transport of gas bubbles in capillaries

John Ratulowski and Hsueh-Chia Chang

Department of Chemical Engineering, University of Notre Dame, Notre Dame, Indiana 46556

(Received 24 May 1988; accepted 13 June 1989)

The pressure drop and wetting film thickness for isolated bubbles and bubble trains moving in circular and square capillaries are computed. An arclength-angle formulation of a composite lubrication equation allows for the numerical matching of the lubrication solution of the transition region to the static profiles away from the channel wall. This technique is shown to extend the classical matched asymptotic analysis of Bretherton for circular capillaries to higher capillary numbers  $Ca$ . More importantly, it allows the study of finite bubbles, which are shown to resemble infinitely long bubbles in film thickness and pressure drop if their lengths exceed the channel width. The numerical study of bubble trains, verified by a matched asymptotic analysis, shows a surprising result that the pressure drop across one member bubble is identical to that of an isolated bubble at low capillary numbers. This analysis of square capillaries neglects azimuthal flow and is only valid for  $Ca > 3.0 \times 10^{-3}$ . Nevertheless the film radius and pressure drop of a bubble traveling in a square capillary above this capillary number are computed. These results are conveniently summarized in a correlation for the apparent viscosity of bubbles as a function of foam texture and capillary geometry and dimension.

## I. INTRODUCTION

Foam has been suggested as a method of mobility control for enhanced oil recovery processes which use gas to displace oil remaining in the reservoir, viz., steam and  $CO_2$  flooding. Because the mobility of foam, quite surprisingly, can be up to a factor of 100 smaller than that of a pure liquid, gravity override, and viscous fingering are greatly reduced. An important problem then becomes quantification of the mobility (or apparent viscosity) of foam within the porous media. A popular model for analyzing the effect of foam texture and quality on the apparent viscosity has been bubble flow in straight capillaries. Although this idealized geometry cannot fully describe the tortuous flow paths in porous media, it allows more detailed and precise experimental scrutiny than more realistic physical models such as bead packs. More importantly, it allows theoretical estimation of the apparent viscosity from first principles via a lubrication analysis. Hirasaki and Lawson<sup>1</sup> have even shown that theoretical results for bubble flow in straight capillaries can sometimes be extended to the more complex problem of foam flow in porous media without significant loss of quantitative accuracy.

The first theoretical treatment of a bubble moving steadily at velocity  $V$  in a circular capillary was done by Bretherton.<sup>2</sup> The analysis is limited to very long bubbles (in fact, infinitely long bubbles) and is an asymptotic result for low capillary number,  $Ca = \mu V / \sigma$ . Park and Homsy<sup>3</sup> formalized Bretherton's approach with the use of perturbation theory and the technique of matched asymptotic expansions. Teletzke<sup>4</sup> extended the analysis to bubbles of finite length. Both Teletzke<sup>4</sup> and Jo<sup>5</sup> examined the effects of intermolecular forces in the thin film region through a disjoining pressure and also the effect of finite dispersed phase viscosity. However, in the case of gas foams one would expect that the assumption of an inviscid gas made by previous investigators is valid. The effect of surfactants on the motion of bubbles has been addressed by several investigators (Schwartz *et al.*,<sup>6</sup> Teletzke,<sup>4</sup> Chen,<sup>7</sup> and Bretherton<sup>2</sup>). While all agree

that surfactant increases the pressure drop across the bubble, no attempt to include surfactant transport was made. Hirasaki and Lawson did model surface transport in the thin film region. However, because the cap region was never addressed, the theory remains incomplete. All these studies are on bubble transport in circular capillaries. It is expected that capillaries with angular cross section would better model the tortuous and irregular flow channels within porous media. Legait<sup>8</sup> has used a static analysis to estimate the pressure drop required to push a bubble through the constriction of a square capillary. Ransohoff and Radke<sup>9</sup> have also computed the resistance to film flow in a family of noncircular capillaries. These computations are used to estimate the bubble breakup rate in constricted square capillaries.<sup>10,11</sup> Nevertheless there exists no study on the pressure drop required to push a single bubble or a bubble train at constant velocity  $V$  through a straight noncircular capillary.

In this paper, we first examine bubbles in circular capillaries. The use of an arclength-angle formulation of a composite lubrication equation is shown to extend the asymptotic results of Bretherton<sup>2</sup> to higher capillary numbers. This approach is similar to that applied to flow of blood cells by Secomb *et al.*,<sup>12</sup> although because of the difference in the free surface conditions, our approach allows complete integration of bubble profiles for infinite and finite single bubbles or bubbles present in bubble trains. Single bubbles or member bubbles present in trains, which are longer than twice the capillary radius, are found to be well approximated by the infinite bubble result. An asymptotic analysis, verified by our numerical result, is developed for long bubbles in bubble trains. From proper matching of the lubrication region to the static nodoid surface of the liquid lamella, simple relationships for pressure drop and film thickness, as functions of the contact radius and capillary number, are derived. These expressions differ from those of Hirasaki and Lawson<sup>1</sup> because a small but finite contact angle exists in our analysis at the edge of the flattened portion of the liquid lamella resulting from pressure jumps across the interface. We then

extend our formulation to bubble flow in square capillaries. As a result of the neglect of azimuthal pressure gradient and velocity, we are only able to compute the film thickness and pressure drop of a long bubble for capillary numbers above  $3.0 \times 10^{-3}$ . We then summarize our results in correlations on how the apparent viscosity of bubble flow in capillaries depends on foam texture and pore geometry and dimension.

## II. LUBRICATION ANALYSIS

Consider a gas bubble surrounded by a wetting fluid moving in a straight capillary of arbitrary cross section with a characteristic half-width  $R$ . The two geometries addressed here, circular and square capillaries, are shown in Fig. 1. The gas bubble may be isolated or part of a bubble train in which individual bubbles are flattened against one another and separated by thin liquid films. The thin liquid film and the plateau border region near the channel wall is called a liquid lamella. In porous media, the characteristic diameter  $2R$  of the flow channels is very small. Therefore the analysis is restricted to channels sufficiently small such that the Bond number  $\Delta\rho g R^2/\sigma$ , is much smaller than unity. (For a typical pore dimension of  $40\ \mu\text{m}$ , the Bond number is approximately  $5 \times 10^{-4}$ .) This implies that the two fluids are neutrally buoyant and the cross section of the air-liquid interface is either axisymmetric or possesses certain symmetries with respect to the center axis, such that the vertical direction is not discernable. We shall only consider bubbles moving with constant speed  $V$  characterized by the capillary number  $\text{Ca} = \mu V/\sigma$  with  $\mu$  being the viscosity of the wetting phase.

At low  $\text{Ca}$ , the front and rear regions of the interface profile are nearly static profiles. We shall show that they are spherical caps for isolated bubbles and nodoidal surfaces for bubble trains. Near the channel wall is a region where both viscous and capillary forces are important. Previous investigators<sup>2,3</sup> have named this region the transition region. For very long bubbles, the transition region merges into a region of uniform film thickness. This uniform film region is not present for short bubbles.

We begin by imposing the usual lubrication assumption that the characteristic variation in the axial flow direction is

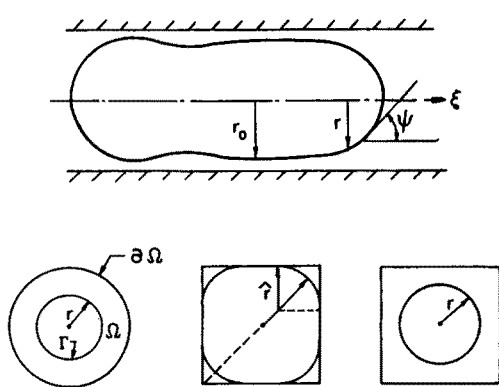


FIG. 1. An isolated bubble moving in a straight capillary of circular or square cross section. The cross-section interfacial positions are shown with circular capillaries of unit radius and square capillaries of unit half-width.

much smaller than the transverse variations in the transition region. In our case, this corresponds to the requirement that the characteristic length of the transition region be much longer than the characteristic film thickness surrounding the bubble. Then a simple order-of-magnitude analysis of the continuity equation stipulates that the flow field is unidirectional in the axial direction to leading order in the film parameter  $f$ , which is the ratio between the transverse characteristic length  $\epsilon$  and the axial characteristic length  $\delta$ ,  $f = \epsilon/\delta \ll 1$ . If one scales all coordinates by the channel half-width  $R$  (which is the capillary radius for a circular capillary and half the channel height for a square capillary), the axial velocity  $w$  by the bubble speed  $V$ , and pressure by  $\sigma/R$ , the creeping flow equations of motion to leading order in  $f$  are

$$\text{Ca} \nabla_{\perp}^2 w = \frac{\partial p}{\partial z}, \quad (1a)$$

$$\nabla_{\perp} p = 0. \quad (1b)$$

(See Chang<sup>13</sup> for a standard asymptotic expansion derivation of this lubrication formulation.) The operator  $\nabla_{\perp}$  is the del operator in the transverse coordinates. Note that all inertial effects are negligible since the typical Reynolds number in a pore is less than  $10^{-4}$ . This certainly satisfies the stipulation that the Reynolds number be of zeroth order in the film number in the derivation of Eq. (1). These equations are essentially two-dimensional generalizations of the one-dimensional equations derived by Park and Homsy,<sup>3</sup> Chang,<sup>13</sup> and Wilson<sup>14</sup> for a planar geometry (Hele-Shaw cell and plate withdrawal problems) using similar scaling arguments.

Boundary conditions to (1) include the usual no-slip condition on the channel wall  $\partial\Omega$  (see Fig. 1),

$$w = 0 \quad \text{on } \partial\Omega \quad (2)$$

and the normal and tangential stress balance on the interface  $\Gamma$ . To leading order in  $f$ , the normal stress balance is simply the two-dimensional neutrally buoyant Laplace-Young equation

$$p = -\kappa \quad \text{on } \Gamma, \quad (3)$$

where  $\kappa$  is the dimensionless normal curvature of the interface. Note that Eq. (1b) stipulates that the pressure is only a function of the axial coordinate  $z$ . This implies that  $\kappa$  is independent of the transverse directions and is constant at every axial cross section. The interfacial cross section  $\Gamma$  then consists of segments of circular arcs since the circle is the only constant curvature in two dimensions. We shall refer to the local radius of curvature as  $r$  or  $\hat{r}$  (see Fig. 1) and it is a function only of the axial coordinate resulting from the pressure variation by viscous dissipation described by the lubrication equations in (1). To leading order in  $f$ , the tangential stress balance for a mobile surface simply reduces to (Chang<sup>13</sup>),

$$w_n = 0 \quad \text{on } \Gamma, \quad (4)$$

where  $n$  denotes the normal derivative.

It is also of interest to note that Eqs. (1a) and (3) stipulate the order assignments of the axial and transverse length scales,  $\delta$  and  $\epsilon$ , respectively, for very thin films. Equation (1a) requires that  $\epsilon^2/\delta \sim O(\text{Ca})$ . For extremely thin films

( $f \ll 1$ ), in the transition region the curvature  $\kappa$  of (3) in the transition region is dominated by the axial curvature with negligible transverse curvature. Since the axial curvature is of  $O(\epsilon/\delta^2)$  in this thin film limit, Eq. (3) implies that  $\epsilon/\delta^2 \sim O(1)$ . These two stipulations then imply that

$$\delta \sim O(Ca^{1/3}), \quad (5a)$$

$$\epsilon \sim O(Ca^{2/3}), \quad (5b)$$

$$f = \epsilon/\delta \sim O(Ca^{1/3}). \quad (5c)$$

Hence  $Ca$  is required to be small for the lubrication approximation ( $f \ll 1$ ) to be valid. The above order assignments are only valid when the film is extremely thin because the order assignment for the curvature,  $O(\epsilon/\delta^2)$ , is only valid in this limit. For infinitely long bubbles, this occurs at vanishing  $Ca$  and (5) breaks down at larger values of  $Ca$ . For very short bubbles, a thin film does not exist and (5) is not appropriate at all. However, even though (5) is not the correct order assignment when the film is not sufficiently thin, our lubrication equation is still valid provided  $Ca$  and  $f$  are moderately low. In fact, one of our objectives is to investigate the behavior at larger values of  $Ca$ .

The order assignment (5b) for the transverse film thickness also indicates that the characteristic film thickness is of  $O(Ca^{2/3})$  at vanishing  $Ca$ , which is consistent with Bretherton and Park and Homsy's results for circular capillaries. Also, pressure drop resulting from viscous dissipation at the limit of zero capillary number can also be estimated from Eq. (5). The viscous dissipation can be simply obtained by applying the divergence theorem to (1a),

$$\Delta p \sim Ca \int w_n |_{\partial\Omega} dx,$$

where the integral is carried out over the transition regions since there is no flow in the stagnant uniform region and viscous effects are negligible in the static cap region. Using the assignments of (5), one concludes that, in the limit of vanishing  $Ca$ ,

$$\Delta p \sim O(Ca^{2/3}) \quad (6a)$$

and the characteristic film thickness

$$h_\infty \sim O(Ca^{2/3}), \quad (6b)$$

which are again consistent with Bretherton's leading-order estimates.

The reason foam has such a low mobility is evident from (6a) for this thin film limit of a capillary model. If a circular capillary contains only the liquid phase undergoing Hagen-Poiseuille flow, the dimensional pressure drop across a capillary length of  $l_T$ , when the liquid is traveling at a constant average velocity of  $V$ , is  $8\mu l_T V / R^2$ . If a series of  $n_B$  bubbles exists in the same length of capillary and travel at the same speed  $V$ , the pressure drop is, from (6a), approximately  $n_B \sigma Ca^{2/3} / R$ . (A more precise computation will be carried out in subsequent sections.) Hence the apparent viscosity of foam relative to the liquid, which is simply the ratio of the pressure drops, is of order  $(n_B R / l_T) Ca^{-1/3}$ . Given that the bubble lengths are typically of the same order as the capillary radius  $R$ ,  $n_B R / l_T \sim O(1)$ , and given that the typical porous media conditions are  $10^{-7} < Ca < 10^{-3}$ , the apparent viscosity of foam is between a factor of 10–100 larger than pure

liquid from this order-of-magnitude argument! This is consistent with pressure drop measurements in bead packs.<sup>1</sup> Of course, the pressure drop across one bubble given by (6a) is a constant independent of the bubble length, while the pressure drop for pure liquid is dependent on the length  $l_T$ . Hence the apparent viscosity of foam is approximately linearly dependent on the texture or the number of bubbles per unit length  $n_B / l_T$ . The reason the pressure drop across a bubble is independent of the bubble length is because there is no dissipation in the middle stagnant film region, which is the major portion of the bubble and can be of arbitrary length. The only viscous dissipation occurs at the transition region whose length is independent of the bubble length. Since the film is so thin in this region, wall stress is enormous and it accounts for the larger pressure drop required to push a bubble at constant speed. A more detailed derivation of the apparent viscosity will be given in the final section, after the pressure drops have been computed.

Since  $p$  is only a function of  $z$ , Eq. (1b) is an inhomogeneous Laplace equation for  $w$  in the transverse coordinates for every axial location with boundary conditions (2) and (3). The solution to  $w$  is then related to the following "fundamental" solution  $\Phi$  within the liquid region  $\Omega$  (see Fig. 1),

$$\nabla_{\Pi}^2 \Phi = -1 \quad \text{in } \Omega, \quad (7a)$$

$$\Phi = 0 \quad \text{in } \partial\Omega, \quad (7b)$$

$$\Phi_n = 0 \quad \text{on } \Gamma. \quad (7c)$$

Given the interface cross section  $\Gamma$  at a particular axial location, the axial velocity is then given by

$$w = \frac{dp}{dz} \Phi. \quad (7d)$$

Hence the volumetric flow rate  $q'$  through the cross section, relative to a fixed laboratory reference frame, is

$$q'(z) = \int_{\Omega} w d\Omega = -K \frac{dp}{dz}, \quad (8)$$

where  $K$  is a dimensionless local flow coefficient defined by

$$K = \int_{\Omega} \Phi d\Omega. \quad (9)$$

This coefficient varies as a function of  $z$  as the interface cross section  $\Gamma$  varies. However, one can often parameterize all possible interfacial cross sections by the radius of curvature  $r$  (or  $\hat{r}$ ) in Fig. 1, provided a given geometry of the interface is assumed. For example,  $\Gamma$  is always circular for circular capillaries and the two geometries depicted in Fig. 1 will be used to model interfaces in square capillaries. In these cases,  $K$  can be related to  $r$  (or  $\hat{r}$ ) directly by solving  $\Phi$  in an appropriate geometry. For example, the circular capillary requires the solution of  $\Phi$  in an annulus of unity outer radius and varying inner radius  $r$ .

Since the bubble is moving steadily (without change of shape) with a constant dimensionless velocity  $Ca$ , with respect to a moving coordinate

$$\xi = z - Ca t, \quad (10)$$

where  $t$  is a dimensionless time scaled with respect to  $R\mu/\sigma$ , the volumetric flow rate  $q$  must be a constant,

$$q = q' - Ca A = \text{const}. \quad (11)$$

In Eq. (11),  $A$  is the area of the cross section liquid flow fraction  $\Omega$ , which is a function of  $z$  or  $\zeta$ . Obviously,  $A(z)$  can also be related to the local radius of curvature  $r(z)$  if a model for the interface  $\Gamma$  is assumed. The volumetric flow rate  $q'$ , with respect to the fixed laboratory frame, is also a function of  $z$ . However, if there exists an axial position where  $q'$  vanishes exactly, which from (8) also implies that the local pressure gradient is zero, and if the cross section liquid flow area at this point is  $A_0$ , then

$$q = -\text{Ca} A_0 = q' - \text{Ca} A. \quad (12)$$

This stagnant region exists at the middle of an infinitely long bubble, which deposits a stationary (in the fixed laboratory frame) uniform film. Hence there is no bypass of liquid around the moving bubble. The area  $A_0$  then corresponds to the flow area at the middle of the infinitely long bubble. However, for finite bubbles,  $q$  is always smaller in magnitude than  $\text{Ca} A_0$ , indicating a finite amount of liquid bypass around the bubble ( $q' > 0$ ). In this case,  $q$  is just a constant negative "bypass" flow rate in the moving coordinate. For these finite bubbles, the film thickness is defined by the shortest distance between the interface and the channel wall.

Substituting (8) into (12), one obtains

$$\frac{dp}{d\zeta} = -\frac{q + \text{Ca} A(r)}{K(r)}, \quad (13)$$

where the moving coordinate flow rate  $q$  is  $-\text{Ca} A_0$  for infinite bubbles and a negative bypass flow rate for finite bubbles. The value of  $q$  remains to be determined at a given  $\text{Ca}$ .

It remains to relate  $p$  to  $r$  through the normal stress condition in (3). The complete curvature in terms of the local radius of curvature is

$$\kappa = -r''/(1+r'^2)^{3/2} + 1/r(1+r'^2)^{1/2}, \quad (14)$$

where primes denote differentiation with respect to the axial coordinate  $\zeta$ . [For the nonaxisymmetric square capillaries,  $\hat{r}$  will replace  $r$  in (14)]. However, in the transition region,  $r' \sim O(\epsilon/\delta) \sim O(\text{Ca}^{1/3})$  and  $r \sim r_0 \sim 1$ , where  $r_0$  is the radius of curvature of the stagnant region. Hence the lubrication approximation in the transition region yields

$$p = -\kappa = r'' - 1/r_0. \quad (15)$$

Substituting (15) into (13) yields a third-order equation in  $r$ , which completely describes the interface profile in the transition region. The boundary conditions for this third-order equation are that the interface must match into static caps of constant but different curvatures at the front and back of the bubbles as  $r$  approaches zero. The curvatures of these static caps are then given by Eq. (14) for constant  $\kappa$ 's. This matching is classically done by the method of matched asymptotic expansions.<sup>3</sup> However, if we retain the complete static curvature Eq. (14) and the lubrication Eq. (13) in a single set of composite equations, all terms that are important in both the transition and static cap regions are included. This set of equations may be integrated through the transition region to the cap regions with the matching occurring internally. The set of composite equations does reduce to the proper limits in each region for low  $\text{Ca}$ . In the transition region, both  $r'$  and  $K(r)$  are small [of orders  $\text{Ca}^{1/3}$  and  $\text{Ca}^2$ , respectively, from (5) and (8)]. Consequently, Eq.

(14) reduces to Eq. (15) and Eq. (13) is important in this region. In the static cap region  $r'$  is not small and  $K(r)$  is  $O(1)$ . Hence Eq. (14) remains unchanged and the pressure gradient is small at  $O(\text{Ca})$ . [In the cap region  $A$  is also  $O(1)$ .] Hence  $p$  is approximately constant and the axisymmetric Laplace-Young equation of (14) is recovered.

There are several numerical advantages for carrying out the matching internally. In the studies of infinitely long bubbles in circular capillaries, Bretherton<sup>2</sup> and Park and Homsy<sup>3</sup> integrate the lubrication equation both forward and backward from the middle flat-film region corresponding to  $A_0$  in Eq. (12) and examine the limiting parabolas traced out by  $r$  as the film height  $h = 1 - r$  approaches infinity and the third derivative of  $r$  vanishes. These parabolas are then matched into the static caps. In the case of finite bubbles, there exists no flat-film region as an initial condition for the integration. One must actually shoot from one bubble cap to another. This cannot be easily done with matched asymptotic expansions. In our formulation, it becomes a relatively easy two-point boundary value problem that is very much suitable for shooting techniques. Also, the static lamellas regions for an axisymmetric bubble train are nodoidal surfaces. Although one can still expand the corresponding elliptic integrals for the matching, as we shall carry out in a subsequent section, the problem can be solved in a much simpler manner with our composite equation since the lamellas are simply described by a different set of boundary conditions. Finally, in approximating (14) by (15) in the lubrication analysis, we have only retained terms of order unity in  $f$ . By using the full expression (14) in the equation, we will retain higher-order terms in the curvature expression. Of course, terms of like order may have been neglected in deriving Eqs. (1), (3), and (4). Nevertheless, as Wilson<sup>14</sup> has demonstrated in his analysis of the plate withdrawal problem, one expects higher-order accuracy if the full curvature expression is used. We shall demonstrate that this is true in our case for at least the film height and pressure drop of circular capillaries by comparing the results from our composite equation to numerical results of the original Stokes flow free surface problem.

To facilitate numerical integration, the composite equations (13) and (14) are expressed in arclength-angle coordinates. The independent variable is the arclength of the interface  $s$  pointing toward the front of the bubble and we define the angle  $\psi$  by (Fig. 1)

$$d\zeta = \cos \psi ds, \quad (16a)$$

$$dr = -\sin \psi ds. \quad (16b)$$

In this coordinate system, the axial component of curvature is simply  $\partial \psi / \partial s$  and the azimuthal component is  $\cos \psi / \hat{r}$ , where  $\hat{r}$  is the radius of the circular arc of  $\Gamma$ , which may be different from the radial interfacial position  $r$  for nonaxisymmetric configurations in square capillaries (see Fig. 1). Equations (13) and (14) in the arclength-angle formulation become

$$\frac{\partial p}{\partial s} = \frac{-\cos \psi [q + \text{Ca} A(\hat{r})]}{K(\hat{r})}, \quad (17a)$$

$$\frac{\partial \psi}{\partial s} = -p + \frac{1}{\hat{r}_0} - \frac{\cos \psi}{\hat{r}}, \quad (17b)$$

$$\frac{\partial r}{\partial s} = -\sin \psi. \quad (17c)$$

Here, we have changed the reference pressure from the pressure in the gas bubble in (3) and (15) to the liquid pressure outside a cylinder of radius  $\hat{r}_0$ . For infinitely long bubbles, which deposit a uniform wetting film,  $\hat{r}_0$  is the azimuthal radius of curvature in the uniform film region. It can then be related to  $q$  through  $A_0$  by Eq. (12). For finite bubbles  $\hat{r}_0$  is never specified independently. It is combined with the variable  $p$ . This presents no difficulties because pressure drop and liquid bypass are independent of the choice of reference pressure and therefore independent of  $\hat{r}_0$ . Another geometry that has been of interest to other investigators<sup>3,15</sup> is the Hele-Shaw cell consisting of two closely spaced flat plates. This geometry is much simpler because it is a planar problem. Therefore the azimuthal curvature is not present. The set of equations, Eq. (17), can be modified to describe this geometry by simply omitting the azimuthal curvature term,  $1/\hat{r}_0 - \cos \psi/\hat{r}$ , in Eq. (17b).

Equation (17) becomes a three-dimensional autonomous dynamical system with state variables  $p$ ,  $\psi$ , and  $r$ . The "time" variable corresponds to the arclength  $s$  along the interface. Since the equation is invariant to a shift in  $s$ , the origin of the arclength  $s$  can be arbitrary. The trajectories of the dynamical system then describe possible bubble profiles. However, the admissible solutions correspond to those that satisfy the static conditions at the front and rear of the bubble. These conditions correspond to specific values of  $\psi$  and  $r$  that the trajectory must intersect. Since specifying  $\psi$  and  $r$  correspond to choosing a straight line in the three-dimensional phase space, admissible solutions correspond to the intersection of the trajectory with a straight line. This intersection of two one-dimensional curves require, in general, the variation of a single parameter. This is the unknown parameter  $q$ , which is adjusted until the intersection occurs. Finally, note that unlike the evolution of dynamical systems, which must always be in the direction of positive time, we will integrate in both the positive and negative  $s$  directions to delineate the front and rear halves of the bubble.

### III. ISOLATED BUBBLES IN CIRCULAR CAPILLARIES

For circular capillaries the fundamental equation, Eq. (7), can be solved analytically, which yields the following flow coefficient:

$$K(r) = (\pi/16)(4r^4 \ln r - 3r^4 + 4r^2 - 1). \quad (18)$$

For slowly moving bubbles in which a very thin film is deposited on the walls, previous investigators<sup>2,4,6</sup> have approximated (18) with the planar result

$$K = (2\pi/3)(1-r)^3 = (2\pi/3)h^3. \quad (19)$$

It is clear that in the limit of  $h = 1 - r \ll 1$ , (18) approaches the planar result of (19).

In this circular geometry, the liquid flow area is simply

$$A(r) = \pi(1-r^2), \quad (20)$$

which completes the derivation of (17), where  $\hat{r} = r$  and

$\hat{r}_0 = r_0$ . In the limit of  $h = 1 - r \ll 1$ , Eq. (17) reduces to the Bretherton equation<sup>2</sup>

$$h''' = 3 \text{Ca}(h - h_\infty)/h^3, \quad (21)$$

where  $h_\infty = 1 - r_0$  is the thickness of the uniform film region. The primes denote derivatives with respect to  $\zeta$ , which also corresponds to  $s$  in this thin film limit since  $\psi \rightarrow 0$ .

The boundary conditions for isolated bubbles are simply the symmetry conditions at the capillary axis

$$\psi = \pi/2, \quad r = 0, \quad \text{at the front tip}, \quad (22a)$$

$$\psi = -\pi/2, \quad r = 0, \quad \text{at the back tip}. \quad (22b)$$

It was previously shown that our composite equation reduces to the Laplace-Young equation in the static limit. The only profile, which is a solution to the Laplace-Young equation and satisfies the symmetry conditions Eq. (22), is a sphere. Hence the arclength-angle formulation of the composite equation reduces in leading order to the Bretherton technique of matching the transition region to the spherical cap of an isolated bubble.

Equation (17) has a unique fixed point at

$$\begin{pmatrix} p \\ \psi \\ r \end{pmatrix} = \begin{pmatrix} 0 \\ 0 \\ r_0 \end{pmatrix}, \quad (23)$$

which in the axisymmetric configuration corresponds to a circular cylinder of radius  $r_0$ . Trajectories entering the fixed point take infinitely long arclength  $s$  to approach it and trajectories emanating from the fixed point take infinitely long  $s$  to leave it. The fixed point then represents the uniform film around the cylinder deposited by an infinitely long bubble. Linearizing (17) about the fixed point one obtains the Jacobian

$$\mathbf{J} = \begin{pmatrix} 0 & 0 & \text{Ca} \gamma \\ -1 & 0 & 1/r_0^2 \\ 0 & -1 & 0 \end{pmatrix}, \quad (24)$$

where  $\gamma$  is a positive constant

$$\gamma = 2\pi r_0/K(r_0). \quad (25)$$

The eigenvalues  $\lambda$  of  $\mathbf{J}$  are determined by the characteristic polynomial

$$\lambda^3 - \text{Ca} \gamma + \lambda/r_0^2 = 0. \quad (26)$$

At  $\text{Ca} = 0$ , there exist three neutrally stable eigenvalues,  $\lambda = 0$  and  $\pm i/r_0$ . For nonzero  $\text{Ca}$  the eigenvalues become

$$\lambda_1 = \alpha^{1/3} + \beta^{1/3} \quad (27a)$$

and

$$\lambda_{2,3} = -\lambda_1/2 \pm (\sqrt{3}/2)(\alpha^{1/3} - \beta^{1/3})i, \quad (27b)$$

where

$$\alpha = \frac{\text{Ca} \gamma}{2} - \left( \frac{\text{Ca}^2 \gamma^2}{4} + \frac{1}{27r_0^6} \right)^{1/2} \quad (27c)$$

and

$$\beta = \frac{\text{Ca} \gamma}{2} + \left( \frac{\text{Ca}^2 \gamma^2}{4} + \frac{1}{27r_0^6} \right)^{1/2}. \quad (27d)$$

Actually, as  $\text{Ca} \rightarrow 0$ ,  $\gamma \text{Ca}$  blows up because of the higher-order viscous effects in this thin film limit. The radius  $r_0$

approaches unity and (19) implies that  $\gamma$  approaches  $3/h_\infty^3$ . Hence, from (6b),  $\gamma \text{Ca}$  is of  $O(\text{Ca}^{-1})$ . Expanding the eigenvalues (27) in this limit of  $\gamma \text{Ca} \gg 1$ , one obtains

$$\lambda_1 \sim (3 \text{Ca})^{1/3}/h_\infty \quad (28a)$$

and

$$\lambda_{2,3} \sim -(3 \text{Ca})^{1/3}(1 \pm \sqrt{3}i)/2h_\infty. \quad (28b)$$

These results can be obtained by perturbing the characteristic polynomial (26) in the limits of  $\text{Ca} \gamma \rightarrow \infty$ . The above results are consistent with the eigenvalues obtained by Bretherton for (21). If one rewrites (21) as a dynamical system by the transformation

$$\begin{pmatrix} x_1 \\ x_2 \\ x_3 \end{pmatrix} = \begin{pmatrix} h \\ h' \\ h'' \end{pmatrix}, \quad (29)$$

then the Jacobian evaluated at the fixed point  $(x_1, x_2, x_3) = (h_\infty, 0, 0)$  yields the characteristic polynomial

$$\lambda^3 - 3 \text{Ca}/h_\infty^3 = 0, \quad (30)$$

which is the limiting form of (26) in the limit of  $\text{Ca} \gamma \sim 3 \text{Ca}/h_\infty^3 \gg 1$ . In fact, the solutions to (30) are simply (28).

Even though the proper viscous limit of  $\text{Ca} \rightarrow 0$  does not correspond to the static limit  $\gamma \text{Ca} \rightarrow 0$  with eigenvalues 0 and  $\pm i/r_0$ , it is instructive to trace the origin of the static eigenvalues since they are related to the static profiles at the tips, which will be useful in subsequent sections. The purely imaginary pair of eigenvalues  $\pm i/r_0$  actually originates from the periodic trajectories around the cylindrical fixed point of the static problem at constant  $p$ . Consider the static submatrix of  $\mathbf{J}$  when the viscous effect is removed by setting  $p$  to zero, this matrix yields a purely imaginary eigenvalue of  $\pm i/r_0$ . This is because the static axisymmetric Laplace-Young equations of (17b) and (17c) for the same curvature  $1/r_0$  ( $p = 0$ ) is exactly integrable to yield a family of solutions parametrized by the parameter  $c$ ,

$$\cos \psi = r/2r_0 + c/r. \quad (31)$$

The solutions corresponding to positive  $c$  are periodic and known as unduloids. Negative  $c$  corresponds to nonperiodic nodoid solutions. The level curves of those solutions are shown in Fig. 2. The case of  $c = r_0/2$  corresponds to the cylindrical fixed point of (23). It is surrounded by a family of periodic unduloidal solutions ( $c > 0$ ) bounded by the spherical solution of the same curvature with  $c = 0$ . The wavelength of the unduloidal solution is given by the following elliptic integral:

$$\tau(c) = 2 \int_{r_1}^{r_2} \frac{dr}{\sqrt{1 - (r/2r_0 + c/r)^2}}, \quad (32)$$

where  $r_{1,2} = (1 \pm \sqrt{1 - 2c/r_0})r_0$ . It can be shown from standard identities on elliptic integrals that

$$\lim_{c \rightarrow r_0/2} \tau = 2\pi r_0. \quad (33)$$

Hence the eigenvalues  $\pm i/r_0$  at  $\text{Ca} = 0$  simply correspond to the limiting wavelength of the unduloid curves near the cylindrical limit.

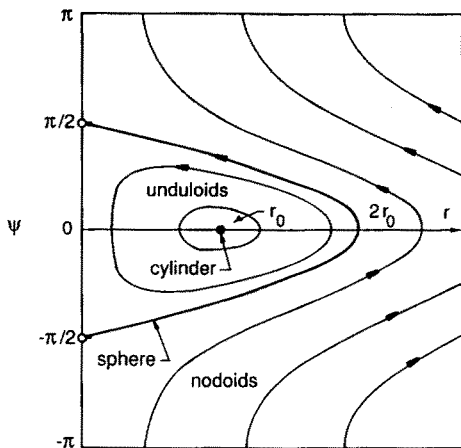


FIG. 2. Level curves of the constant curvature solutions to the axisymmetric Laplace-Young equation. They correspond to a cylinder, a sphere and families of periodic unduloidal and nonperiodic nodoidal surfaces.

As shown by (27) and (28), viscous effects introduce an unstable eigenvalue (in the positive  $s$  direction) to the cylindrical fixed point. The trajectories near the cylindrical fixed point now consist of a real unstable eigenvector and two stable complex eigenvectors. Note that these stability assignments are in the direction of positive arclength. If one shoots in the negative  $s$  direction, these assignments are reversed. Any perturbation of the dynamic system from the cylindrical fixed point will quickly follow in the positive  $s$  direction the unstable eigenvector  $\lambda_1$ , given by

$$u_1 = \begin{pmatrix} \text{Ca} \gamma/\lambda_1 \\ \lambda_1 \\ -1 \end{pmatrix}. \quad (34)$$

The unstable eigenvector soon becomes the one-dimensional curve  $W_u$  in Fig. 3, called the unstable manifold,<sup>17</sup> as it moves farther away from the cylindrical fixed point toward the bubble front in the positive  $s$  direction. This trajectory,  $W_u$ , corresponds to the front half of the bubble and we require it to intersect the line  $\psi = \pi/2$  and  $r = 0$  of Eq. (22) at the tip. This corresponds to the upper end of the spherical

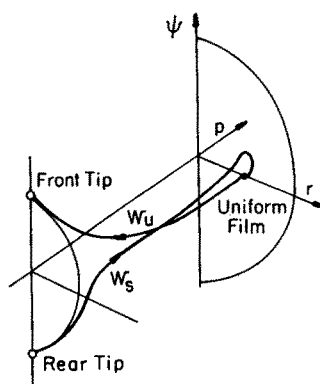


FIG. 3. The front and rear film profiles correspond to the unstable manifold  $W_u$  and the stable manifold  $W_s$  of the cylindrical fixed point at the flat-film region with zero pressure. The manifolds approach a spherical solution with  $p$  near 2. (The front and rear pressures are slightly different but this is not apparent with the scale of the drawing).

solution. As shown in Fig. 3, the intersection of two curves in the phase space requires, generically, the variation of one parameter  $q$ , the unknown liquid flow rate. It is also clear from (17) that the intersection with  $r = 0$  can only occur tangentially. Hence, by iterating on  $q$  for a given  $\text{Ca}$ , one can readily determine the correct  $q$ , which satisfies the tip condition. The film profiles of Eqs. (17) are integrated with a fourth-order predictor-corrector method. A Newton scheme is used to update iterates of  $q$  and a first-order continuation technique is employed to predict new initial guesses for  $q$  as the parameter  $\text{Ca}$  is changed. At the end of

the iteration, one obtains  $q$  and the front pressure drop  $p_f$  as functions of  $\text{Ca}$ .

To construct the rear half of the bubble, one needs to integrate in the negative  $s$  direction from the cylindrical fixed point. This reverses the stability assignment of the eigenvalues in (27) and the trajectory leaves the cylindrical fixed point in a two-dimensional manifold  $W_s$  (a trajectory on the two-dimensional manifold is shown in Fig. 3) corresponding to the complex eigenvalues  $\lambda_{2,3}$ . This  $W_s$  is tangent to the unstable eigenspace at the fixed points. This two-dimensional eigenspace is described by the two eigenvectors

$$\begin{pmatrix} p \\ \psi \\ r \end{pmatrix} = \begin{pmatrix} 0 \\ 0 \\ r_0 \end{pmatrix} + \delta \left[ \begin{pmatrix} \text{Ca} \gamma \lambda_R / (\lambda_R^2 - \lambda_I^2) & & \\ & -\lambda_R & \\ & & 1 \end{pmatrix} + \omega \begin{pmatrix} \text{Ca} \gamma \lambda_I / (\lambda_R^2 - \lambda_I^2) \\ \lambda_I \\ 0 \end{pmatrix} \right], \quad (35)$$

where  $\omega$  specifies the angle of departure from the fixed point relative to the two unstable eigenvectors and  $\delta$  is the perturbation from the fixed point, which is arbitrary as long as it is small. A one-dimensional trajectory on the two-dimensional manifold  $W_s$  is now required to intersect tangentially the line  $\psi = -\pi/2$  and  $r = 0$  on the spherical static curve. This again requires the variation of one parameter. Since  $q$  has been determined by the forward shooting iteration, we vary  $\omega$  instead until the back condition is satisfied. At this point, the rear pressure drop  $p_r$  is also determined at the given  $\text{Ca}$  and the total pressure drop  $\Delta p = p_r - p_f$  can be obtained. Note that in Fig. 3, the front tip and rear tip should be tangent to two different  $p$  planes corresponding to constant  $p_f$  and  $p_r$  for the front and rear liquid pressures of the static cap regions ( $p_f < p_r$ ). However, the difference is so small it is not differentiated in the figure for clarity.

The above eigenvalue analysis has two important implications. Since the fixed point is unstable in both positive and negative  $s$  directions, it is extremely difficult to shoot toward the fixed point against the flow of the unstable eigenvector or eigenvectors. This explains why the solution of the Bretherton equation has traditionally involved shooting from the flat-film region to the two caps. It would be difficult to shoot from the caps to the flat-film region. Second, since the unstable eigenvalue is real in the positive  $s$  direction and the unstable eigenvalues are complex in the negative  $s$  direction, we expect the profile of the front half to be monotonically increasing while the back half should be undulating. In fact, the characteristic wavelength of the waves is simply  $2\pi/[\sqrt{3}(\alpha^{1/3} - \beta^{1/3})/2]$  from (27b). In the thin film limit, the wavelengths are of  $O(\text{Ca}^{1/3})$  from (28b) and (6b).

In Fig. 4, we present our flat-film thickness  $h_\infty = 1 - r_0$  for both the axisymmetric and planar geometries. It is seen that for  $\text{Ca} < 0.01$ , our result approaches the Bretherton limit

$$r_0 = 1 - 1.3375 \text{ Ca}^{2/3}. \quad (36)$$

However, for  $\text{Ca} > 0.01$ , our formulation deviates significantly from the Bretherton limit and follows the exact result of the creeping flow free surface problem by the finite differ-

ence of Reinelt and Saffman<sup>15</sup> up to  $\text{Ca} \sim O(10^{-1})$ . Lu and Chang<sup>16</sup> have also solved the two-dimensional Stokes problem with a boundary integral numerical scheme and obtained results almost identical to those of Reinelt and Saffman. Figure 4 demonstrates that the arclength-angle formulation of the composite equation significantly extends the Bretherton asymptotic result for film thickness to higher  $\text{Ca}$  values. In Fig. 5, we show the front and back bubble

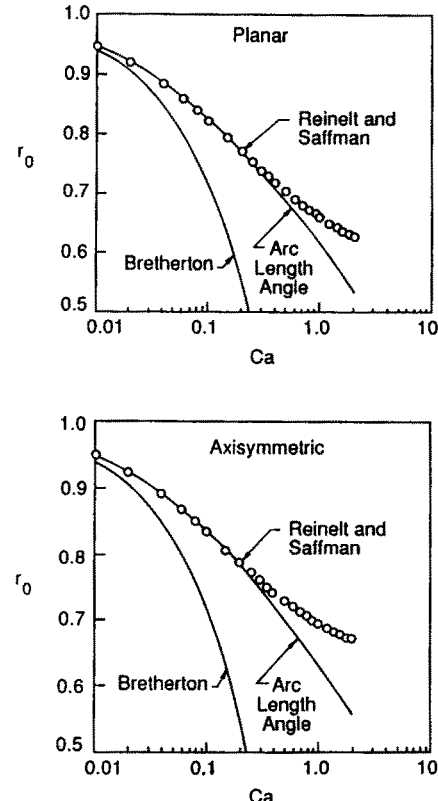


FIG. 4. Computed film thickness as compared to Bretherton's low  $\text{Ca}$  asymptotic result and Reinelt and Saffman's numerical result for the planar and axisymmetric geometries. The composite approach is in agreement with the exact results up to  $\text{Ca} = 0.2$ .

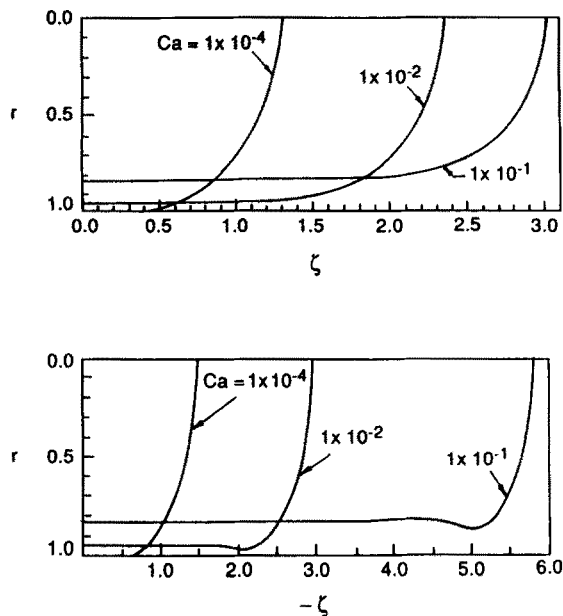


FIG. 5. Front and back film profiles for very long bubbles at various capillary numbers. The monotonic front profile and the undulating back profile are evident.

profiles for various  $\text{Ca}$  values. The undulating back profile is evident. In Fig. 6, the computed total pressure drop across the bubble for both axisymmetric capillaries and planar Hele-Shaw cells are compared to the Bretherton asymptotic

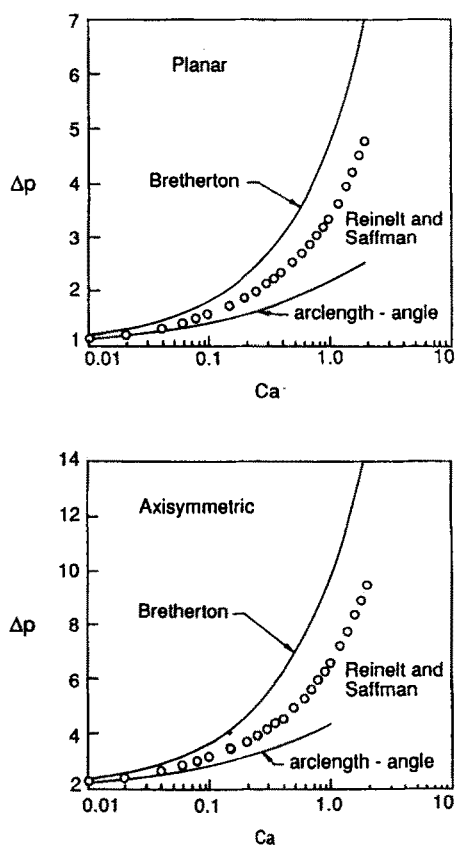


FIG. 6. Computed pressure drop compared to Bretherton's low  $\text{Ca}$  asymptotic result and Reinelt and Saffman's numerical results for the planar and axisymmetric geometries. The composite approach is in agreement with the exact results up to  $\text{Ca} = 0.06$ .

limit and Reinelt and Saffman's exact results.<sup>15</sup> Unlike the film thickness shown in Fig. 4, the arclength-angle formulation of the composite equation seems to overcorrect the Bretherton result such that a larger deviation from the exact result is observed at lower  $\text{Ca}$  values. However, the range of  $\text{Ca}$  where the computed pressure drop is valid is still extended. The total pressure drop for  $\text{Ca} < 0.1$  may be correlated as

$$\Delta p = 9.40 \text{ Ca}^{2/3} - 12.6 \text{ Ca}^{0.95}. \quad (37)$$

The composite formulation introduces a correction to the asymptotic of nearly  $O(\text{Ca})$ . This is the next-order correction one would expect from the asymptotic analysis. In the limit of low  $\text{Ca}$ , Eq. (37) approaches Bretherton's low  $\text{Ca}$  limit

$$\Delta p = 9.40 \text{ Ca}^{2/3}. \quad (38)$$

For finite bubbles, we initiate the integration at each bubble tip toward the opposite one with the symmetry conditions of Eq. (22). The finite arclength of the entire bubble implies that the cylindrical fixed point, which requires an infinite amount of arclength to traverse, is never part of the bubble profile. In Fig. 7(a) the trajectory for a very short bubble, for which  $r$  is always smaller than  $r_0$ , is shown. Figure 7(b) corresponds to a trajectory for a finite bubble with length greater than twice the tube radius. The rotation about the fixed point corresponds to the characteristic wavy rear profile in the long bubbles. This rotation has been exaggerated in Fig. 7(b) for clarity. It is actually very near the fixed

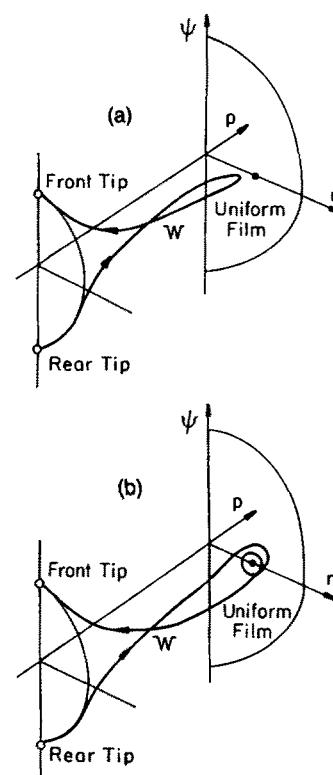


FIG. 7. The film profiles of short bubbles do not traverse the cylindrical fixed point at zero pressure. The shorter profile in (a) does not have undulating profiles as seen in (b) because it does not come close enough to the uniform film cylindrical fixed point to feel the effects of the complex eigenvalues.

point, resulting in small-amplitude oscillations in film thickness. Again, the system is solved with a standard Newton scheme. A first-order continuation technique is used to estimate new initial guesses for  $q$  as either bubble axial cross-sectional area or  $\text{Ca}$  is changed. The axial cross section is determined by

$$a_c = \int_{\text{bubble}} \pi r d\xi. \quad (39)$$

In Fig. 8, bubble profiles for a short bubble of constant volume moving at three different speeds is shown. At slow speeds the bubble flattens and forms an elliptical shape. As speed increases the bubble deforms to an elongated bullet shape, which is qualitatively similar to the solutions of the two-dimensional Stokes equation by Chang and Lu.<sup>16</sup> In Fig. 9, the bypass flow rate and pressure drop across a bubble is plotted as a function of bubble area for two  $\text{Ca}$ . It is evident that at low  $\text{Ca}$ ,  $q$  quickly converges to the stagnant film limit of infinitely long bubbles in Eq. (12) and Fig. 4, which corresponds to the Bretherton solution (36) in the thin film limit. The transition is not a sharp at higher  $\text{Ca}$ . However, for fairly short bubbles with lengths only slightly in excess of twice the channel half-width  $R$ , the bypass flow rate  $q$  is well approximated by the infinite bubble results. Similar behavior for the total pressure drop was found, as shown in Fig. 9. Consequently, for bubbles with volume larger than  $4\pi R^3/3$ , the infinite bubble results are adequate approximations for bypass flow and pressure drop.

#### IV. BUBBLE TRAINS IN CIRCULAR CAPILLARIES

Within porous media, foams of high quality (low liquid content) are commonly encountered. Here the bubbles are flattened against one another so that adjacent bubbles are separated only by a thin lamella similar to those surrounding soap bubbles. Near the wall is a larger liquid region, which is the counterpart of plateau borders in bulk foams. Without the stabilizing effects of surfactant molecules, the liquid within the lamellas will eventually drain out and the two

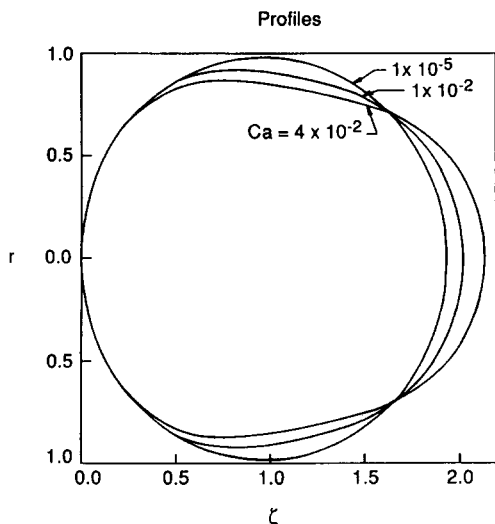


FIG. 8. The bubble profiles of a constant volume short bubble with dimensionless cross-sectional area  $A/R^2$  of 3.0 at three velocities.

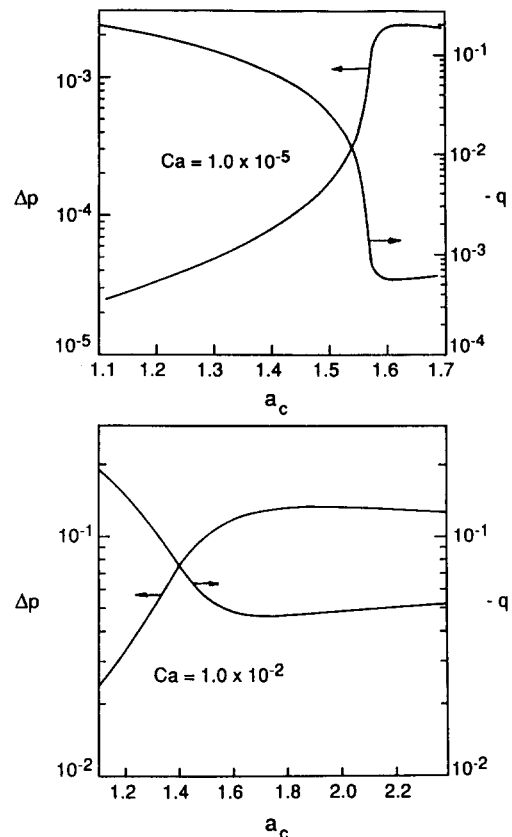


FIG. 9. Bypass flow rate and pressure drop for short bubbles as functions of the bubble volume at two different  $\text{Ca}$  values. Note that both  $q$  and  $\Delta p$  overshoot the infinitely long bubble values and approach them from the other side.

interfaces will coalesce. Such coalescence, however, occurs over a large time scale and in the study of the transport of bulk foam, it is typical to assume quasisteady lamellas.<sup>18</sup> In porous media flow and in laboratory studies of bubble transport in capillaries, however, sufficient surfactant has been added to eliminate this coalescence phenomenon entirely.<sup>1,19</sup> In our own laboratory, these lamellas are observed to sustain a pressure differential in the air pressures of two adjacent bubbles essentially indefinitely as it travels through the capillary.<sup>20</sup> These surfactant molecules will reduce the local surface tension and if a gradient in their surface concentration exists, a surface-tension-driven flow occurs, which will change the pressure drop and film thickness results. We shall not address the effect of this surface tension variation in the present model. However, we shall assume that the lamellas have been stabilized and can sustain a pressure drop across them. We shall, however, show that this pressure drop across the lamellas is of  $O(\text{Ca}^{2/3})$  and is small at low bubble speeds. This implies that the lamellas are only slightly displaced from the vertical at the point of contact ( $\psi_c \sim \pi/2$  in Fig. 10).

Consider the bubble train shown in Fig. 10. The train consists of a large number of either identical short bubbles or long bubbles of arbitrary volume. The volume of the long bubbles need not be a constant because as in the isolated bubble case, bubbles that start to flatten against the tube wall (bubble length  $> 2R$ ) are adequately approximated by an

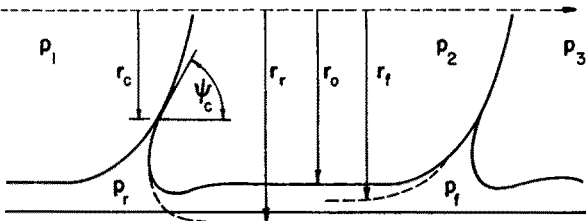


FIG. 10. Schematic of a bubble train. The contact angle  $\psi_c$  and contact radius  $r_c$  for the lamellas are shown. Limiting radial positions  $r_f$  and  $r_s$  are the extrapolation of the static lamellas and  $r_0$  is the flat-film cylinder radius.

infinitely long bubble.<sup>19</sup> However, each liquid lamella in the train is assumed to be identical. Because of the assumption of identical lamellas, the gas pressure must increase by a constant amount as one passes through each lamella. Hence the gas pressure of each bubble in Fig. 10 must be related by

$$p_1 - p_2 = p_2 - p_3 = \dots = p_i - p_{i+1}. \quad (40)$$

The reason that identical lamellas are assumed is to provide "periodic" boundary conditions for the lubrication equations (17). If the pressure drop across each lamella is not identical or if the air pressure is not even monotonically decreasing in the flow direction, our model is then a "statistically averaged" idealized bubble train. The same periodic assumptions have traditionally been assumed to study random systems such as bulk foam<sup>18</sup> and diffusion in porous media.<sup>21</sup>

Consider the rear of the middle bubble in the train of Fig. 9. A force balance over the control volume containing the thin liquid film yields

$$(p_1 - p_2)\pi r_c^2 = 2(2\pi r_c \cos \psi_c). \quad (41)$$

The additional factor of 2 on the right-hand side arises because the thin liquid film is comprised of two gas-liquid interfaces. The angle  $\psi_c$  is the contact angle at the point  $r = r_c$ . Let  $p_r$  be the liquid pressure at the rear of the second bubble and  $p_f$  the liquid pressure at the front of the bubble. If the lamellas are identical,

$$p_1 - p_r = p_2 - p_f. \quad (42)$$

Note that the rear and front liquid pressures of the second bubble are simply the front and rear liquid pressures of the first and third bubbles, respectively. Equation (42) implies that if the bubble train is moving such that there is viscous dissipation to cause a finite liquid pressure drop  $p_r - p_f$  across the bubble, there must be an accompanying air pressure drop  $p_1 - p_2$  of the same magnitude across the lamella under our identical lamella assumption. This, in turn, implies that the contact angle  $\psi_c$  cannot be  $\pi/2$  unless the bubbles are isolated ( $r_c = 0$ ). In fact, combining Eqs. (41) and (42) are rearranging yields

$$\cos \psi_c = (r_c/4)\Delta p, \quad (43)$$

where  $\Delta p = p_r - p_f$  is the total liquid pressure drop across a bubble. Note that we expect  $\Delta p$  to be of  $O(\text{Ca}^{2/3})$  from (6a) and since  $0 < r_c < 1$ , (43) implies that  $\cos \psi_c$  is of  $O(\text{Ca}^{2/3})$  or smaller. Hence, in the thin film limit,  $\psi_c$  is almost vertical.

The constraint imposed by (43) implies that we cannot vary  $r_c$  and  $\psi_c$  independently since the computed pressure

drop must satisfy (43). Instead, specifying  $r_c$ , which measures the degree of compression between the bubbles and Ca fully determines the problem. This then requires an additional iteration loop. For a given Ca and  $r_c$ ,  $\psi_c$ ,  $q$ , and  $\omega$  for a long member of the bubble train are iterated such that at the bubble ends

$$\psi = \psi_c, \quad r = r_c \quad \text{at the front,} \quad (44a)$$

$$\psi = \psi_c - \pi, \quad r = r_c \quad \text{at the rear,} \quad (44b)$$

and Eq. (43) is satisfied after  $\Delta p$  is obtained. To facilitate this three-dimensional iteration problem, we utilize a first-order continuation scheme starting from the isolated bubble result ( $r_c = 0$ ) of the previous case for a given Ca and continue into the finite  $r_c$  region. Convergence is then achieved with a standard Newton iteration scheme. In Fig. 11, we present the flat-film thickness result normalized with respect to the isolated bubble film thickness for mobile bubbles for various  $r_c$  and Ca values. It can be seen from Fig. 11 that the normalized film thicknesses collapse to single curves for both the planar geometry without the azimuthal curvature term in (17b) and axisymmetric geometry. The normalized film thickness for the Ca range of  $10^{-6}$ – $10^{-2}$  fall on these two curves. Surprisingly, the results for the planar geometry corresponding to Hele-Shaw flow and the axisymmetric geometry for capillary flow do not converge, even in the low Ca limit. This result is unexpected because for isolated bubbles in the limit of low Ca, when a very thin film is deposited, the film thickness for both geometries converge to the same value.<sup>2</sup> This has been seen in Figs. 4 and 6 from our numerical integration of the composite equation for isolated bubbles. Obviously, there is a qualitative difference between the axisymmetric bubble train and the isolated bubble. Moreover, the computed  $\Delta p$  as a function of Ca and  $r_c$ , as shown in Fig. 11, show little dependence on  $r_c$  at sufficiently low Ca.

These surprising results for bubble trains may be confirmed by a matched asymptotic analysis similar to that of Bretherton for isolated long bubbles at low Ca. Carrying out the following transformation,  $\eta = h/h_\infty$  and  $\xi = \xi h_\infty / \text{Ca}^{1/3}$ , Bretherton's equation (21) can be conveniently scaled such that Ca and  $h_\infty$  do not appear explicitly.

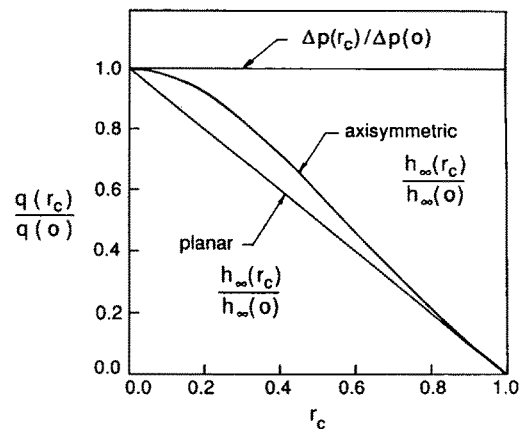


FIG. 11. Pressure drop and uniform film thickness for a bubble train normalized with respect to an isolated bubble as functions of the contact radius  $r_c$ . Both planar and axisymmetric pressure drops show no dependence on  $r_c$ .

This universal form is

$$\frac{d^3\eta}{d\xi^3} = \frac{3(\eta - 1)}{\eta^3}. \quad (45)$$

Note that in our composite equation formulation of (17), the capillary number could not be conveniently scaled out of the problem as it is in (45). Consequently, an iterative solution of (17) for film height is required at each capillary number while a single integration of (45) will be shown to be sufficient to completely describe all behavior in the thin film limit. The additional computational complexity is the price for extending the analysis to finite bubbles and higher Ca values, where a thin film does not exist.

Bretherton has integrated (45) from the flat-film region where  $\eta = 1$  and  $d\eta/d\xi = d^2\eta/d\xi^2 = d^3\eta/d\xi^3 = 0$  and obtained the behavior of  $\eta$  as  $\xi$  approaches positive and negative infinity. Regardless of the direction, the third derivative vanishes asymptotically as  $\eta$  increases, as is evident from (45). The quadratic behaviors of  $\eta$  as  $\xi \rightarrow \pm \infty$  are determined by Bretherton as

$$\eta \sim (\eta''_\infty/2)(\xi - \xi_i^0)^2 + \eta_i^{\min}, \quad (46)$$

where  $\eta''_\infty$ ,  $\xi_i^0$  and  $\eta_i^{\min}$  are constants and the subscript  $i$  denotes  $r$  and  $f$  for bubble rear and front in the negative and positive  $\xi$  directions, respectively. Note that the coefficient of the second-order term  $\eta''_\infty$  is independent of direction. The parameters have been obtained by Bretherton to be

$$\eta''_\infty = 1.338, \quad (47a)$$

$$\eta_f^{\min}\eta''_\infty = 3.72, \quad (47b)$$

$$\eta_r^{\min}\eta''_\infty = -0.98. \quad (47c)$$

The locations of the minima  $\xi_i^0$  are inconsequential, as Bretherton has noted, and we shall show below that the same is true for bubble trains. In the original variables of (21), (46) becomes

$$\lim_{\xi \rightarrow \pm \infty} h(\xi) = (\eta''_\infty \text{Ca}^{2/3}/2h_\infty)(\xi - \xi_i^0)^2 + \eta_i^{\min}h_\infty, \quad (48)$$

where  $\xi_i^0 = \xi_i^0 h_\infty / \text{Ca}^{1/3}$  but is again inconsequential.

The film profile in the transition region represented by (48) must be matched into the static bubble front and rear. Bretherton determines his results [(36) and (38)] for isolated infinitely long bubbles at low Ca by matching (48) to spheres at the front and the rear of the bubble. We shall match (48) onto static surfaces that pass through the boundary conditions (44) at the contact points. Consider the planar geometry corresponding to the Hele-Shaw flow first, the front and rear lamellas must then be circular arcs. However, because of boundary conditions (44), these circular arcs do not have centers at the channel center axis. Instead, they lie below the center axis by a distance  $a$ . Consider the front lamella. Simple geometrical arguments dictate that

$$(r_c - a)/R_f = \cos \psi_c, \quad (49)$$

where  $R_f$  is the radius of the front circular arc. However, from the static force balance across the lamella, Eq. (43), and noting that  $\Delta p \sim O(\text{Ca}^{2/3})$  in the thin film limit, one concludes from (43) and (49) that  $\cos \psi_c \sim O(\text{Ca}^{2/3})$  and

$$a \sim r_c + O(\text{Ca}^{2/3}), \quad (50)$$

since  $R_f \sim O(1)$ . A similar analysis of the rear lamella also yields (50) for the center of the rear circular arc.

Extending the above circular arcs beyond the lamellas region, such that the resulting circles have their minima at  $\xi_r^0$  and  $\xi_f^0$  of the minima of the film profiles of (48) for the rear and front, one obtains

$$(1 - h - a)^2 + (\xi - \xi_i^0)^2 = R_i^2, \quad (51)$$

where  $R_i$  denotes  $R_f$  and  $R_r$ , radii of curvature of the front and rear lamellas. Expanding (51) for small  $h \sim O(\text{Ca}^{2/3})$  and using (50), one obtains

$$h \sim \frac{(\xi - \xi_i^0)^2}{2(1 - r_c)} + \frac{(1 - r_c)}{2} - \frac{R_i^2}{2(1 - r_c)}. \quad (52)$$

Matching (52) to (48), one obtains from the first term for both the front and the rear,

$$h_\infty(r_c) = (1 - r_c)\eta''_\infty \text{Ca}^{2/3} = (1 - r_c)h_\infty(0), \quad (53)$$

which is in exact agreement with our numerical results of Fig. 11. Hence the film thickness decreases resulting from the compression at the bubble ends, as one would intuitively expect. Matching the constant terms of (52) and (48) for both the rear and the front yields

$$R_f^2 = (1 - r_c)^2 - 2\eta_f^{\min}h_\infty(1 - r_c), \quad (54a)$$

$$R_r^2 = (1 - r_c)^2 - 2\eta_r^{\min}h_\infty(1 - r_c). \quad (54b)$$

Note that since  $\eta_f^{\min}$  is positive and  $\eta_r^{\min}$  is negative by (47), the rear lamella has a larger radius of curvature. From (54), one obtains

$$R_r^2 - R_f^2 = 2h_\infty(1 - r_c)(\eta_f^{\min} - \eta_r^{\min}). \quad (55)$$

The liquid pressure drop  $\Delta p$  across one bubble member is  $1/R_f - 1/R_r$ . However, since both  $R_r$  and  $R_f$  are of  $O(1)$  in this thin film limit, we can define

$$R_i = 1 - r_c - b_i, \quad (56)$$

where  $b_i \sim O(\text{Ca}^{2/3})$  and  $b_f > 0$  and  $b_r < 0$ , indicating the front lamella has a radius of curvature smaller than the rear radius. Hence

$$\Delta p \sim b_f - b_r. \quad (57)$$

However, substituting (56) into (55) yields, to leading order,

$$b_f - b_r \sim h_\infty(1 - r_c)(\eta_f^{\min} - \eta_r^{\min}). \quad (58)$$

Hence, in the thin film limit, (58) and (53) yield

$$\Delta p(r_c) \sim h_\infty(0)(\eta_f^{\min} - \eta_r^{\min}) = \Delta p(0) \quad (59)$$

and the pressure drop is independent of the degree of compression between bubbles, as measured by  $r_c$ . This is consistent with our numerical result in Fig. 11. Note that this is not equivalent to saying that the pressure drop is independent of the texture or quality of the bubble train. The pressure drop across an entire train of  $n_B$  member bubbles is  $n_B \Delta p$  and is hence linearly proportional to the number of bubbles. Hence, if the texture or quality of the bubble varies such that there is a larger number of bubbles per unit length, the pressure drop or the apparent viscosity will increase accordingly.

The static lamellas for the axisymmetric circular capillary are more complex than the circular arcs of the planar

geometry. This renders the matching of the lubrication solution (48) more involved. These axisymmetric constant-curvature lamellas, which pass through points specified by the boundary conditions (44), are described by the axisymmetric Laplace–Young solutions of (31), with  $r_0$  replaced by  $R_f$  and  $R_r$ , the front and rear total radius of curvature. These solutions are depicted in Fig. 2. Since the boundary conditions (44) indicate that, at a given value of  $r = r_c$ , the angle  $\psi_c$  is larger than that for a sphere at the small radial position resulting from the compression, the parameter  $c$  must be negative and the front and rear lamellas are then the nodoidal surfaces depicted in Fig. 2. In cylindrical  $r$ - $\xi$  coordinates, these surfaces are represented by the following elliptic integral:

$$\xi - \xi_i^0 = - \int_{r_i}^r \frac{\alpha_i(r^2 - \beta_i^2) dr}{[r^2 - \alpha_i^2(r^2 - \beta_i^2)]^{1/2}}, \quad (60)$$

which replaces the much simpler  $r$ - $\psi$  representation of (31). In (60), we have imposed the condition that  $\psi$  vanishes at the minima  $\xi_i^0$  of the lubrication solution (48). This and boundary conditions (44) then specify the parameters  $\alpha_i$  and  $\beta_i$  (and the radii of curvature  $R_r$  and  $R_f$ ),

$$\alpha_i = (r_i \pm r_c \cos \psi_c)/(r_i^2 - r_c^2) = 1/2R_i, \quad (61a)$$

$$\beta_i^2 = r_i^2 - r_i/\alpha_i, \quad (61b)$$

where again the subscript  $i$  denotes front and rear  $r$  lamellas and the negative and positive signs correspond to front and rear lamellas. The radial positions  $r_f$  and  $r_r$  in (61) are the values of  $r$  at  $\psi = 0$  and  $-\pi$ , respectively, of the nodoidal level curves of the Laplace–Young equation shown in Fig. 2. Hence they are the limiting radial positions of the extensions of the lamellas into the thin film region, as shown in Fig. 10. These limiting radial positions of the static lamellas must be matched to (48).

Since  $r_i$  are of  $O(1)$ , we define

$$1 - r_i = c_i, \quad (62)$$

where  $c_i \ll 1$  is of  $O(\text{Ca}^{2/3})$  from (6). Substituting (62) into (60) and carrying out an expansion of the elliptic integral for small  $c_i$ , one obtains, after considerable algebra that also imposes the condition  $\cos \psi_c \sim O(\text{Ca}^{2/3})$  (see the thesis of Ratulowski<sup>19</sup> for details),

$$h(\xi) = 1 - r \sim \frac{1}{2} [(1 + r_c^2)/(1 - r_c^2)] (\xi - \xi_i^0)^2 - c_i, \quad (63)$$

which describes the limiting behaviors of the front and rear lamellas as they are extended into the flat-film region ( $\psi \rightarrow 0$  or  $-\pi$ ). Note that while this expression is identical to the planar result (52) at  $r_c = 0$  corresponding to the isolated bubble limit, they are distinct when  $r_c \neq 0$ . Hence, while the film thickness result of Bretherton (36) is valid for both geometries, this is not true for the bubble trains. This qualitative difference between the planar and axisymmetric geometry arises from the requirement that the lamellas be nodoidal surfaces instead of spheres when the bubbles are pressing against each other. While spheres behave like circles near the minima  $\xi_i^0$ , nodoidal surfaces do not behave like circular arcs in the same limit, as is evident from Fig. 2.

Matching (63) to (48), one obtains

$$h_\infty(r_c) = [(1 - r_c^2)/(1 + r_c^2)] \eta_\infty'' \text{Ca}^{2/3} = [(1 - r_c^2)/(1 + r_c^2)] h_\infty(0), \quad (64a)$$

$$c_i = -\eta_i^{\min} h_\infty = -\eta_i^{\min} [(1 - r_c^2)/(1 + r_c^2)] h_\infty(0). \quad (64b)$$

Hence the film thickness result is consistent with our numerical result in Fig. 10. The liquid pressure drop can also be extracted from  $c_i$ . From (61a),  $\alpha_i$  is half the total front and rear curvatures. Since the air pressure is constant, the liquid pressure drop is then

$$\Delta p = 2(\alpha_f - \alpha_r). \quad (65)$$

Eliminating  $\psi_c$  from the force balance across the lamellas (43) and carrying out an expansion of  $\alpha_i$  to leading order in  $c_i$ , one obtains

$$\Delta p \sim 2(c_r - c_f) [(1 + r_c^2)/(1 - r_c^2)] + O(|c_i|^2). \quad (66)$$

Substituting (64), the liquid pressure drop is then obtained

$$\Delta p(r_c) \sim 2(\eta_f^{\min} - \eta_r^{\min}) h_\infty(0) = \Delta p(0), \quad (67)$$

which is independent of the contact radius, as we have seen from our numerical integration of the composite equations.

## V. SQUARE CAPILLARIES

Our models of the interface  $\Gamma$  of an infinitely long bubble in a square capillary are as depicted in Fig. 1. Near the ends, where there is a large liquid flow area  $A(r)$ ,  $\Gamma$  is axisymmetric and is described by a circle with radius  $r$ . Near the middle of the bubble, where there is little liquid flow or liquid flow area,  $\Gamma$  can be nonaxisymmetric and is then consisted of four disjoint circular arcs of constant radius  $\hat{r}$ . We disregard the thin films where  $\Gamma$  touches the four side walls. This non-axisymmetric model is certainly valid when the fluid is completely static as in the flat-film region since circular arcs, which are tangent to the walls, are the only solutions to the two-dimensional Laplace–Young equation. However, if the liquid is flowing at the point when the profile changes from the axisymmetric configuration to the nonaxisymmetric configuration, the fluid within the films of  $\Gamma$  must be considered. In this case, the normal curvature  $\kappa$  in (3) will not be constant in the transverse cross section since  $\kappa$  is zero at the thin film and  $\kappa$  is  $1/\hat{r}$  at the circular arcs. This also implies that there is an azimuthal pressure gradient that induces azimuthal flow to drain the fluid in the film. All these are inconsistent with our unidirectional flow lubrication approximation of Sec. II. Hence we only expect our model to be valid for relatively large  $\text{Ca}$  when either the entire bubble profile is in the axisymmetric configuration or when only a small segment in the stagnant middle of the infinite bubble is in the nonaxisymmetric configuration. For low  $\text{Ca}$ , when a large portion of the bubble, including the transition region where the liquid is flowing, is expected to be in the nonaxisymmetric region, our model will fail. We shall proceed with our numerical analysis of the composite equation for square capillaries and show that a failure to converge does occur at low  $\text{Ca}$  values. Certainly, the expected low  $\text{Ca}$  behaviors of (6) are never realized. Nevertheless we are able to obtain some results at larger  $\text{Ca}$  values.

The fundamental solution of Eq. (7) for square capillaries cannot be solved analytically. Instead, the flow coefficient  $K(r)$  is obtained with a Galerkin spectral technique. A quadrant of  $\Omega$  in Fig. 1 is mapped into a rectangle. The map is singular at the square corners. However, if the corners are smoothed such that symmetry is preserved and the first derivative of the wall with respect to the azimuthal coordinate is continuous, the singularity is removed. Convergence has been duly checked with result to the number of modes used in the spectral expansion and the smoothing approximation.<sup>19</sup> The numerical results for the smoothed corners are estimated to be within 5% of that for the actual sharp cornered geometry. The computed flow coefficient in the square geometry for the mobile interface is adequately fitted by

$$K(r) = \exp(-2.092 - 1.099r + 1.982r^2 - 5.311r^3) \quad (68)$$

for an axisymmetric gas core  $r < 1$ . For the nonaxisymmetric interface, the gas bubble flattens against the channel walls leaving liquid regions in the corner defined by circular arcs with radius  $\hat{r}$ . Through simple geometric arguments  $\hat{r}$  may be related to the position of the interface along a diagonal of the square channel in Fig. 1 by

$$\hat{r} = (\sqrt{2} - r)/(\sqrt{2} - 1). \quad (69)$$

The flow coefficient for this configuration is then

$$K(\hat{r}) = \hat{r}^4 K(1), \quad (70)$$

where  $K(1)$  is the flow coefficient of Eq. (68) at  $r = 1$ . Hence a numerical solution for the fundamental solution  $\Phi$  is unnecessary for the nonaxisymmetric case.

The liquid flow areas of the two configurations are

$$A(r) = 4 - \pi r^2, \quad \text{axisymmetric}, \quad (71a)$$

$$A(\hat{r}) = 4\hat{r}^2 - \pi\hat{r}^2 \quad \text{nonaxisymmetric}. \quad (71b)$$

Equations (68)–(71) then completely specify the composite equations (17) with boundary conditions (22) for isolated bubbles. Whenever  $r$  or  $\hat{r}$  increases beyond unity during the shooting procedure, the nonaxisymmetric or axisymmetric configuration is then assumed. The forward shooting portion encounters no difficulty. An entirely axisymmetric front half is obtained for  $Ca > 0.04$  and the computed film thickness can be fitted by

$$h_\infty = 1 - r_0 = 0.6933 - 0.0977 \ln Ca, \quad (72)$$

where  $A_0 = 4 - \pi r_0^2$  is the area of the stagnant region and  $r_0$  replaces  $\hat{r}_0$  in (17b). In this region, the entire bubble is axisymmetric. For  $Ca$  less than 0.04, a converged front profile is obtained for all  $Ca$  but the bubble is nonaxisymmetric in the flat-film region and becomes axisymmetric closer to the front. If the static nonaxisymmetric configuration is restricted to the flat-film region, which is completely stagnant, our theory remains valid since the nonaxisymmetric circular arcs are good models for the static regions and the numerical scheme should continue to converge. If, however, the nonaxisymmetric segment becomes dominant and intrudes into the nonstatic regions at the ends, the model will break down and numerical convergence is not obtained. Indeed, the backward shooting portion, using the  $q$  and  $r_0$  values determined from the forward shooting portion, fails to converge

below  $Ca = 3.0 \times 10^{-3}$ . This probably represents the limit of validity of our model because of the neglect of azimuthal flow in the film region. For  $Ca > 3.0 \times 10^{-3}$ , the computed liquid pressure drop is depicted in Fig. 12 and it can be correlated by

$$\Delta p = a Ca^n, \quad (73)$$

where  $a = 3.14$  and  $n = 0.14$  for completely axisymmetric bubbles and  $a = 12.2$  and  $n = 0.55$  for nonaxisymmetric bubbles.

## VI. APPARENT VISCOSITY

An apparent viscosity of bubbles and bubble trains in arbitrary channels can be easily defined with an extension of the method of Hirasaki and Lawson.<sup>1</sup> This viscosity would be that which would produce the same single-phase flow rate in a circular tube of equivalent hydraulic radius  $R$  and is therefore defined by the Hagen-Poiseuille relation

$$\mu_A = (R^2/8V)(\Delta\hat{p}_T/l_T), \quad (74)$$

where  $\Delta\hat{p}_T$  is the dimensional pressure drop across the channel,  $V$  is the bubble velocity, which is related to the superficial gas velocity, and  $l_T$  is the channel length.

The total pressure drop  $\Delta\hat{p}_T$  is then separated into two contributions,

$$\Delta\hat{p}_T = \Delta\hat{p}_s + \Delta\hat{p}_B, \quad (75)$$

where  $\Delta\hat{p}_s$  is the dimensional pressure drop in the liquid slugs separating the isolated bubbles and  $\Delta\hat{p}_B$  is the pressure drop across all the bubbles in the channel length  $l_T$ . From the dimensional version of (8) for single-phase flows ( $r$  or  $\hat{r}$  equals zero) and using the average slug velocity  $V_s$  to scale  $w$  and  $\mu V_s/R$  to scale  $p$  in (8), one obtains

$$\Delta\hat{p}_s = \mu V_s A(0) l_s / K(0) R^2, \quad (76)$$

where  $l_s$  is the total slug length and  $A(0)$  and  $K(0)$  are the dimensionless flow area and flow coefficient of (18), (20), (68), and (71) for the pure liquid case ( $r = 0$ ). The total bubble pressure drop is simply

$$\Delta\hat{p}_B = n_B \Delta p \sigma / R, \quad (77)$$

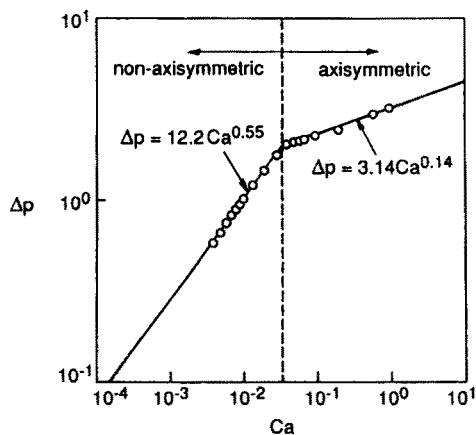


FIG. 12. Total pressure drop across a bubble in a square capillary as a function of  $Ca$ . The circles are numerical data and the straight lines are fitted curves.

where  $n_B$  is the total number of bubbles in  $l_T$  and  $\Delta p$  is given by (37) and (73) for circular and square capillaries; assuming, of course, the bubble lengths exceed  $2R$  and also invoking the bubble train results of (67). Combining (76) and (77) in (75), (74) yields the normalized apparent viscosity,

$$\frac{\mu_A}{\mu} = \frac{1}{8} \left[ \left( \frac{A(0)}{K(0)} \right) \left( \frac{l_s}{l_T} \right) \left( \frac{V_s}{V} \right) + \left( \frac{n_B R}{l_T} \right) \left( \frac{\Delta p}{Ca} \right) \right]. \quad (78)$$

Note that the bubble lengths do not affect the apparent viscosity for the mobile bubbles studied here. Note also the linear dependence on the bubble texture  $n_B/l_T$ . Most importantly, we see that the liquid slug contribution is of  $O(1)$  since  $V_s \sim V$  and  $(l_s/l_T) \sim O(1)$ , but the bubble contribution is much larger than  $O(1)$  because of the term  $(\Delta p/Ca)$  and the expressions (37) and (73). Hence, except in the case

of very coarse bubble texture ( $Rn_B/l_T \rightarrow 0$ ), the liquid slug contribution can be neglected and the apparent viscosity is exactly linear with respect to  $(n_B/l_T)$ . This is certainly the case for the most common flow configuration of foam in porous media—bubble trains whose bubble members are separated by lamellas instead of liquid slugs. Equation (78) represents our final correlation for the apparent viscosity of bubbles and bubble trains in circular and square capillaries. It should prove useful for correlating the apparent mobility of foam in porous media. If one assumes a pseudohomogeneous Darcy flow model for foam,

$$\mathbf{V} = -(\kappa/\mu) \nabla \hat{p}, \quad (79)$$

where  $\mu$  is the liquid viscosity, then the apparent mobility is given by

$$\frac{k}{\mu} = \frac{l_T V}{\Delta \hat{p}_T} = \frac{R^2 / \mu}{[(A(0)/K(0))(l_s/l_T)(V_s/V) + (n_B R / l_T)(\Delta p/Ca)]} \quad (80)$$

which is approximately  $(R/\mu)(l_T/n_B)(Ca/\Delta p)$  in most realistic flow conditions. Hence, knowing the foam velocity  $Ca$ , the characteristic pore radius  $R$ , and the foam texture  $(n_B/l_T)$ , the apparent mobility of foam can be obtained by using either (37) and (73) for  $\Delta p$ .

## ACKNOWLEDGMENTS

We are also grateful to D. A. Reinelt for supplying the numerical values of his analysis in Figs. 4 and 6.

This work is partially supported by the Enhanced Oil Consortium of the University of Houston and the National Science Foundation under Grant No. CBT84-51116.

<sup>1</sup>G. J. Hirasaki and J. B. Lawson, Soc. Pet. Eng. J. **25**, 176 (1985).

<sup>2</sup>F. P. Bretherton, J. Fluid Mech. **10**, 166 (1961).

<sup>3</sup>C.-W. Park and G. W. Homsy, J. Fluid Mech. **139**, 291 (1984).

<sup>4</sup>G. F. Teletzke, Ph.D. thesis, University of Minnesota, 1983.

<sup>5</sup>E.-J. Jo, Ph.D. thesis, University of Houston, 1984.

<sup>6</sup>L. W. Schwartz, H. M. Princen, and A. D. Kiss, J. Fluid Mech. **172**, 259 (1986).

<sup>7</sup>J.-C. Chen, J. Colloid Interface Sci. **341**, 109 (1986).

<sup>8</sup>B. Legait, J. Colloid Interface Sci. **96**, 28 (1983).

<sup>9</sup>T. C. Ransohoff and C. J. Radke, J. Colloid Interface Sci. **121**, 392 (1988).

<sup>10</sup>T. C. Ransohoff and C. J. Radke, PCH Physicochem. Hydrodyn. **8**, 255 (1987).

<sup>11</sup>T. C. Ransohoff and C. J. Radke, AIChE J. **33**, 753 (1987).

<sup>12</sup>T. W. Secomb, R. Skalak, N. Özkaya, and J. F. Gross, J. Fluid Mech. **163**, 405 (1986).

<sup>13</sup>H.-C. Chang, Chem. Eng. Sci. **41**, 2463 (1986).

<sup>14</sup>S. D. R. Wilson, J. Eng. Math. **16**, 209 (1982).

<sup>15</sup>D. A. Reinelt and P. G. Saffman, SIAM J. Stat. Comput. **6**, 542 (1985).

<sup>16</sup>W.-Q. Lu and H.-C. Chang, J. Comput. Phys. **77**, 340 (1988).

<sup>17</sup>J. Guckenheimer and P. J. Holmes, Nonlinear Oscillations, *Dynamical Systems and Bifurcation of Vector Fields* (Springer, New York, 1983).

<sup>18</sup>A. M. Kraynik, Annu. Rev. Fluid Mech. **20**, 325 (1988).

<sup>19</sup>J. Ratulowski, Ph.D. thesis, University of Houston, 1988.

<sup>20</sup>S.-S. Ni, M.S. thesis, University of Houston, 1986.

<sup>21</sup>H. Brenner, Philos. Trans. R. Soc. London **297**, 81 (1980).

Copyright © 2003 EBSCO Publishing